

Water content and geotherm in the upper mantle above the stagnant slab: Interpretation of electrical conductivity and seismic P-wave velocity models

Masahiro Ichiki^{a,*}, Kiyoshi Baba^a, Masayuki Obayashi^a, Hisashi Utada^b

^a *Institute for Research on Earth Evolution, Japan Agency for Marine–Earth Science and Technology, Natsushima 2-15, Yokosuka, Kanagawa 237-0061, Japan*

^b *Earthquake Research Institute, University of Tokyo, Yayoi 1-1-1, Bunkyo, Tokyo 113-0032, Japan*

Received 6 December 2004; received in revised form 6 June 2005; accepted 22 September 2005

Abstract

Geotherm and water content profiles in the upper mantle above the stagnant slab of the Pacific back-arc were estimated from the electrical conductivity and seismic P-wave velocity (V_p) structures. The geothermal profiles were determined by using the electrical conductivity and seismic V_p structures, which, assuming a dry harzburgite or a dry pyrolite composition, are designated as electrical and seismic geotherms, respectively. In a deeper part of the upper mantle, neither the dry pyrolite nor the dry harzburgite condition provides consistent electrical and seismic geotherms. This discrepancy can be explained by allowing for a small amount of water (500–1000 ppm H/Si) with the seismic geotherm. In a shallower part of the upper mantle, the electrical and seismic geotherms are consistent with each other within 1500–1700 °C under the dry harzburgite condition, whereas they are inconsistent by more than 100 °C under the dry pyrolite condition. Alternatively, the wet pyrolite condition applied to the deeper part of the upper mantle also satisfies the electrical conductivity and seismic V_p structures in the shallower part.

© 2005 Elsevier B.V. All rights reserved.

Keywords: Water; Back-arc volcanism; Stagnant slab; Harzburgite; Pyrolite; Electrical conductivity; Seismic P-wave velocity

1. Introduction

The presence of active volcanism (Miyashiro, 1986) and stagnant slab in the mantle transition zone (Fukao et al., 1992) are the most outstanding features in the north-eastern part of China (NEC), Pacific back-arc. The origin of the back-arc volcanism has not been resolved, nor is it clear whether the back-arc volcanism is associated with the stagnant slab. Fig. 1 shows schematic images of the proposed hypotheses on the origin of the volcanism. The hot region (Miyashiro, 1986) and hot asthenospheric up-

welling hypothesis (Xu, 2001; Yang et al., 2003) propose a geothermal origin, the harzburgite plume hypothesis (Tatsumi and Eggins, 1995) as chemical/petrological origin. The harzburgite plume hypothesis allows for direct association between the origin of the volcanism and the presence of the stagnant slab: the explanation is that the harzburgite and mid-ocean ridge basalt (MORB) components cause density reversal in the stagnant slab, and a large mass of harzburgite consequently flows up in the upper mantle as a plume. The wet region hypothesis (Iwamori, 1992) postulates that the volcanism is of volatile/water origin.

To estimate geotherm and water content (or hydrogen dissolution) profiles in the upper mantle beneath

* Corresponding author.

E-mail address: ichiki@jamstec.go.jp (M. Ichiki)

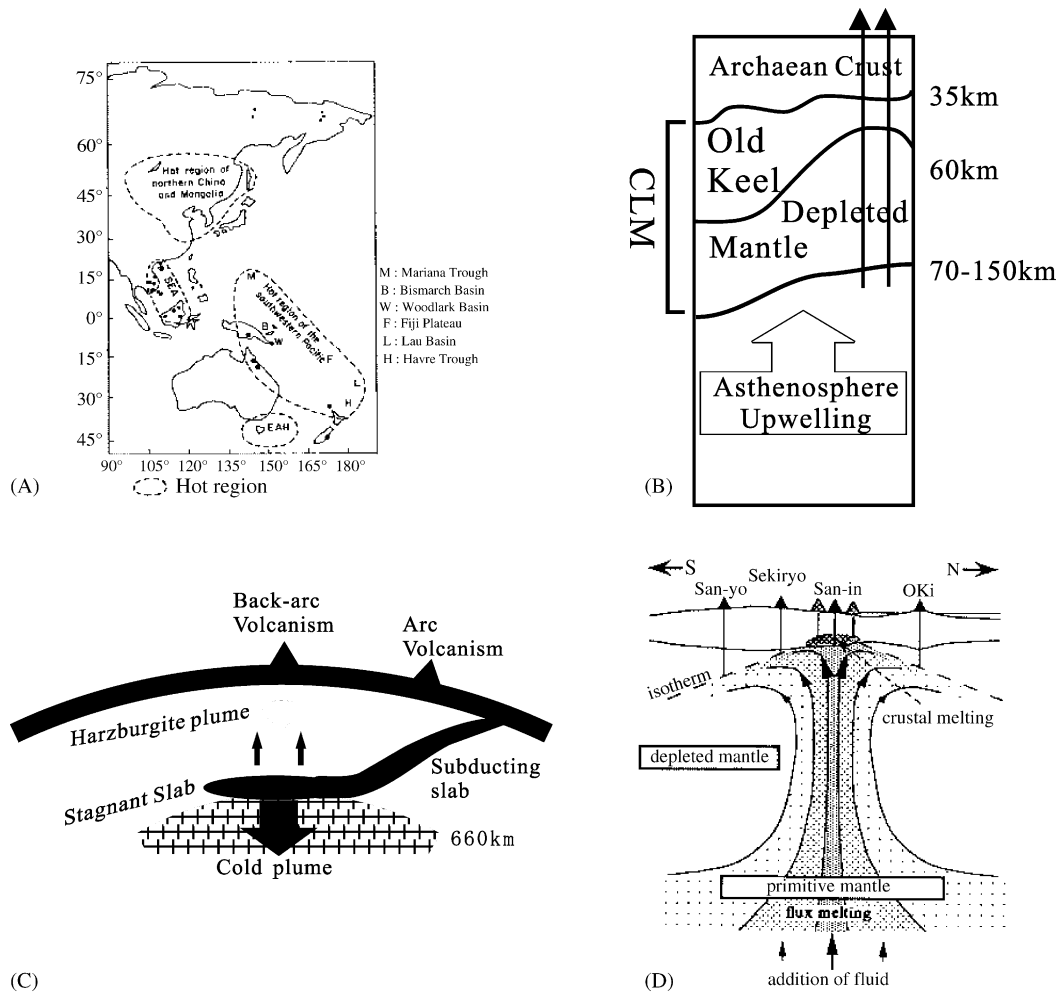


Fig. 1. Hypotheses for origin of the Pacific back-arc volcanism. (A) Hot region hypothesis (Miyashiro, 1986): the Pacific back-arc volcanism took place, when a high geothermal region shifted beneath NEC. This hypothesis presumes that the hot region is distributed around the world. (B) Hot asthenospheric upwelling hypothesis (Xu, 2001): a thermal energy is provided from the deeper mantle. The hot asthenosphere thins the continental lithospheric mantle (CLM) and upwells passively along suture zones. (C) Harzburgite plume hypothesis (Tatsumi and Eggin, 1995): harzburgite mass, which is separated from stagnant slab, rises and the petrological heterogeneity causes solidus temperature decrease in a shallower part of the upper mantle. (D) Wet region hypothesis (Iwamori, 1992): the area beneath the back-arc is under a wet condition, which causes a solidus temperature decrease.

the Pacific back-arc is one of the most effective means for examining the three hypotheses. In order to estimate geotherm and water content profiles, this study utilizes electrical conductivity and seismic P-wave velocity structures. These geophysical parameters depend on temperature, petrological composition, water content and so on. It is still difficult to separate geothermal, petrological and water content anomalies completely in the mantle from geophysical structures. Thus pure olivine mantle composition has been often assumed in order to estimate geotherm and water content in the mantle. Solving the problem in the pure olivine mantle condition, the use of both conductivity and velocity structures is ex-

pected to constrain geotherm and water content in silicates more precisely, considering that the dependency of velocity structure on temperature and on water content is different from that of conductivity (e.g., Fukao et al., 2004). Fukao et al. (2004) estimated mantle geotherms beneath Pacific region from velocity and conductivity structures assuming dry olivine composition. However, Duffy and Anderson (1989) and subsequent studies emphasized the effect of not only olivine but also other silicates on the velocity structure in the upper mantle. It is well known that pyrolite is one of the most suitable standard petrological compositions of the upper mantle (e.g., Ringwood, 1975). Therefore, we employed a pyro-

lite composition rather than a pure olivine as a standard mantle composition in estimating geotherm and water content. Moreover, we took a harzburgite composition as well as a pyrolite composition into account. Because it is possible that harzburgite exists in the target depth range of this study (200–400 km) according to the harzburgite plume hypothesis.

Whereas many seismic tomographic studies have revealed the velocity structure beneath NEC (van der Hilst et al., 1991; Fukao et al., 1992, 2001; Bijwaard et al., 1998), there has been no deep mantle conductivity study. An extensive electromagnetic (EM) observation in the Ocean Hemisphere Project in Japan was carried out in NEC. Ichiki et al. (2001) elucidated the conductivity structure beneath NEC and compared the result with the conductivity models of other tectonic settings. The obtained conductivity structures between 200 and 400 km in depth were as conductive as that beneath the southwestern United States, one of the most active tectonic regions in the world. Moreover, the mantle transition zone was significantly more conductive than those beneath the Pacific ocean (Hawaii), the southwestern United States and Canadian shield. However, comparison among local conductivity structures possibly creates misunderstanding. In other words, the comparison with the standard/averaged global model guarantees the quantitative anomaly. In this paper, the observed EM data are remodeled and the obtained model is compared with the standard global model. Probing the essential anomaly of conductivity, we estimate mantle geotherm and water content profiles.

2. Summary of the electrical conductivity and seismic P-wave velocity structures beneath northeastern China in the Pacific back-arc

The EM data were obtained by applying the Network-MT (magnetotelluric) method (Uyeshima et al., 2001) in NEC. Figs. 2 and 3 show the electrode and geomagnetic observatory locations, and the MT and Geomagnetic Depth Sounding (GDS) response data, respectively. The detailed EM observation and data processing are described in Ichiki et al. (2001). In spite of the different direction along which the telluric field was observed, the shapes of the perpendicular apparent resistivity response curves and the perpendicular phase response curves, respectively, resemble each other. Besides, the amplitudes of the parallel apparent resistivity responses are one to two orders of magnitude smaller than those of the perpendicular responses. We interpreted that (1) the obtained EM response data are regionally one-dimensional affected by galvanic distortion that consists of static shift

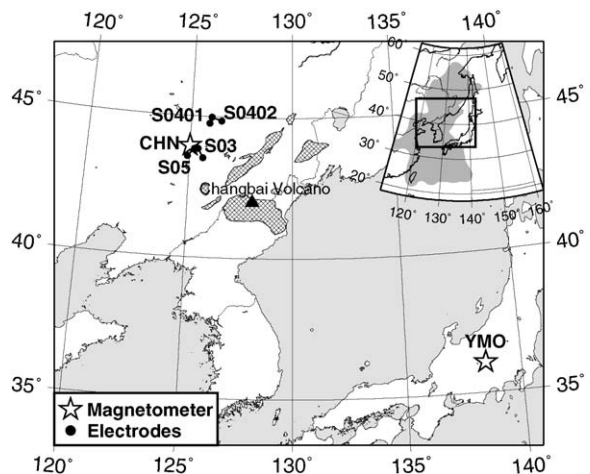


Fig. 2. Electrode and geomagnetic observatory locations. The basalt field is referred to the data of Miyashiro (1986). The mapping of the stagnant slab in the child map is based on the V_p structure presented by Fukao et al. (1992).

and weak or no phase mixing and (2) the static shift is mainly characterized by superficial sediments arranged on the topography. The static shift was overcome by utilizing the GDS responses (e.g., Schultz and Larsen, 1987). The static shift factors were 0.279, 7.11, 32.4 and 6.08 at S03, S0401, S0402 and S05, respectively. Using the obtained EM responses, the remodeling was employed with releasing the smoothness constraint at 400 and 660 km in depth by the Occam inversion (Constable et al., 1987) based on a demonstration by Utada et al. (2003) who have showed that the initial guess allows us to account for the large conductivity jump across 400 km in depth accompanied by olivine-spinel transition (e.g., Xu et al., 1998). The solid lines in Fig. 4 show the conductivity structures obtained by remodeling the EM responses. The previous results obtained without initial guess are also superimposed on Fig. 4 (broken lines). The conductivity change is only a half-order of magnitude or less by incorporating the initial guess. This result suggests that conductivity of the upper mantle beneath this region is comparable to that of the mantle transition zone. Fig. 5 shows the observed EM responses and those calculated from the resultant conductivity structures. Stopping threshold in the Occam inversion is fixed at 1.0 of root-mean-squared (rms) misfit, which is achieved in the analyses of S03, S0401 and S0402 data. The solid and broken lines in Fig. 5 show the EM responses obtained by the remodeling and previous modeling, respectively. The appraisal of the penalty functional leads the different calculated responses in the longer periods. The remodeled results in the longer periods is more fitted to those

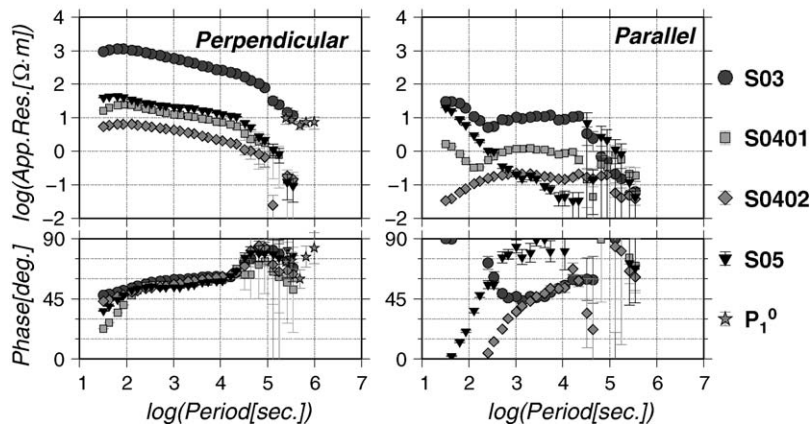


Fig. 3. Apparent resistivity and phase response data with the jackknife errors (Chave et al., 1987). The perpendicular and parallel responses are obtained by rotating magnetic field perpendicular and parallel to the telluric field, respectively. The star symbols show the MT-compatible responses converted from GDS ones at CHN geomagnetic station with approximating the extrinsic geomagnetic field to be P_1^0 harmonic (e.g., Schultz and Larsen, 1987). Circle, square, diamond and reverse triangle symbols represent the apparent resistivity and phase responses at S03, S0401, S0402 and S05, respectively.

of the observed responses than the previous results. The structure of S05 is excluded in following analyses, since the normalized rms misfit calculated from the structure of S05 did not achieve 1.0.

Obtained the optimal one-dimensional structure, we confirmed the necessary condition of the validity of our dimensionality interpretation: we tested whether the static shift and no or weak phase mixing were realized by the superficial sediments arranged on the topography. Three-dimensional modeling (Mackie et al., 1994) was performed with a model in which conductive sediments were superimposed on the resultant one-dimensional conductivity structure. Fig. 6 shows a topographic map around observation sites by the ETOPO2 data. S03 and S05 locate near the boundary of the plain and the mountain range, while S0401 and S0402 locate in the plain region. Fig. 7 represents a central region of the test model. The horizontal mesh size and cell dimension in the central region are $40 \text{ km} \times 40 \text{ km}$ and $68 \text{ km} \times 68 \text{ km}$, respectively. Moreover, additional cells, the horizontal sizes of which are 80, 160, 320 and 640 km, are attached in the outer region. The minimum and maximum vertical mesh sizes are 1 and 12.73 km, and the vertical cell dimension is 168. Before investigating the effect of the conductive sediments, we confirmed that the oceanic effect did not affect the responses. The responses calculated from the model, in which only an ocean bathymetry was incorporated as shown in Fig. 7, coincide with the observed data on which the static shift is corrected. The ocean bathymetry was discretized with 1000 m width referring to ETOPO2. The superficial heterogeneity on land was allowed for in terms of thin sheet conductor with repre-

sentative thickness of 1000 m. The representative conductance of the sedimentary basin and other area were fixed at 1000 S and 0.2 S, respectively, while the conductance of the sedimentary basin almost dominated the results. We calculated the responses at 327,680, 87,380, 21,850 and 4096 s in period. An upward static shift for S03 and downward static shifts for S0401, S0402 and S0501 are expected to be modeled by the superficial sediments arranged on the topography. The calculated apparent resistivity and phase response data are represented on Fig. 5. The calculated shift senses coincide with the expected ones, and phase response data are almost consistent with the observed ones. These shifts are qualitatively consistent with values of the static shift estimated by matching the GDS responses. This result indicates that our interpretation of dimensionality is appropriate.

The obtained conductivity structures, which were designated as the Pacific back-arc structures (PBAs), were compared with two kinds of standard mantle conductivity structures; one obtained by the field data (FLDs) proposed by Utada et al. (2003), the other inferred from the laboratory experiments (LABs). Fig. 8 represents the comparison of PBAs, FLDs and LABs. The PBAs are larger than the standard structures by about 1.5 orders at between 200 and 400 km in depth, whereas the conductivity structures of the mantle transition zone between 400 and 660 km in depth are essentially the same within the confidence level. We regarded the conductivity structure obtained from EM data in the Pacific by Utada et al. (2003) as the standard structure obtained by field data, based on the fact that Kuvshinov et al. (2005) compiled various kinds of EM

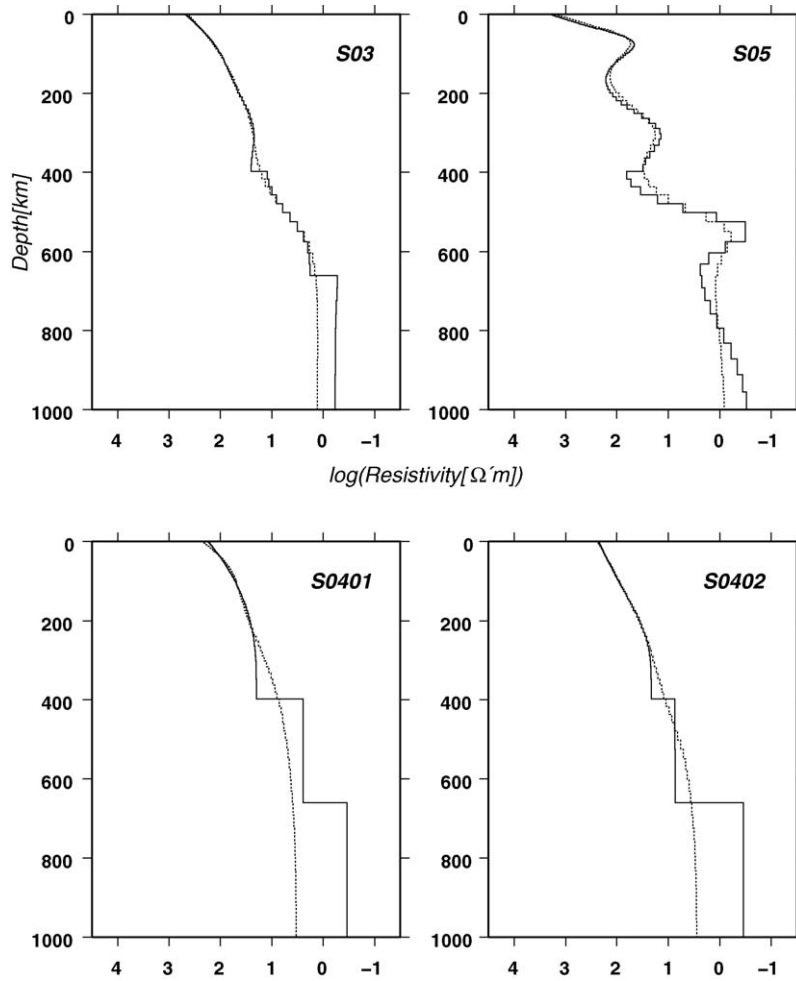


Fig. 4. One-dimensional conductivity structures at all sites obtained by the Occam inversion [Constable et al. \(1987\)](#). The solid lines show the resultant structures with releasing the smoothness constraint at 400 and 660 km in depth. The dotted lines show the conductivity structures obtained without the initial guess.

world-wide data sets and concluded that this model is also valid for a global model. With regard to LABs, we recalculated a conductivity structure assuming a pyrolite composition ([Ringwood, 1975](#)) with incorporating pyroxene-garnet transition ([Irifune et al., 1986](#); [Akaogi et al., 1987](#)), as is represented in [Fig. 9](#). [Fig. 9](#) also shows a standard geothermal profile used in the calculation of LABs, which was proposed by [Ito and Katsura \(1989\)](#). The procedure for calculating LABs constitutes calculating the conductivity of each silicate by Arrhenius law and combining those conductivities by a mixing law to calculate the bulk pyrolite conductivity. The Arrhenius law is described as

$$\sigma = \sigma_0 \exp\left(-\frac{\Delta H}{kT}\right) \quad (1)$$

where σ_0 , ΔH , k and T are pre-exponential factor, activation enthalpy, Boltzman constant and absolute temperature, respectively. Activation enthalpy, ΔH , is defined as $\Delta H = \Delta U + P\Delta V$, where ΔU , P and ΔV are internal energy, pressure and activation volume, respectively. Since $P\Delta V$ is much smaller than ΔU , the activation enthalpy is often determined to be independent of pressure in the laboratory experiments. The activation enthalpies and pre-exponential factors are controlled by chemical composition. Here, clinopyroxene (Cpx) and Ca-majorite were replaced by ($\text{En}_{92}\text{Fs}_8$) and ($\text{Py}_{90}\text{Alm}_{10}$), respectively, because of the lack of experiments on the influence of calcium on conductivity. The pre-exponential factor 56,500 S/m and enthalpy 2.60 eV were applied to the garnet laboratory data ([Poe et al., 2002](#)). For other pre-exponential factors and activation enthalpies of sili-

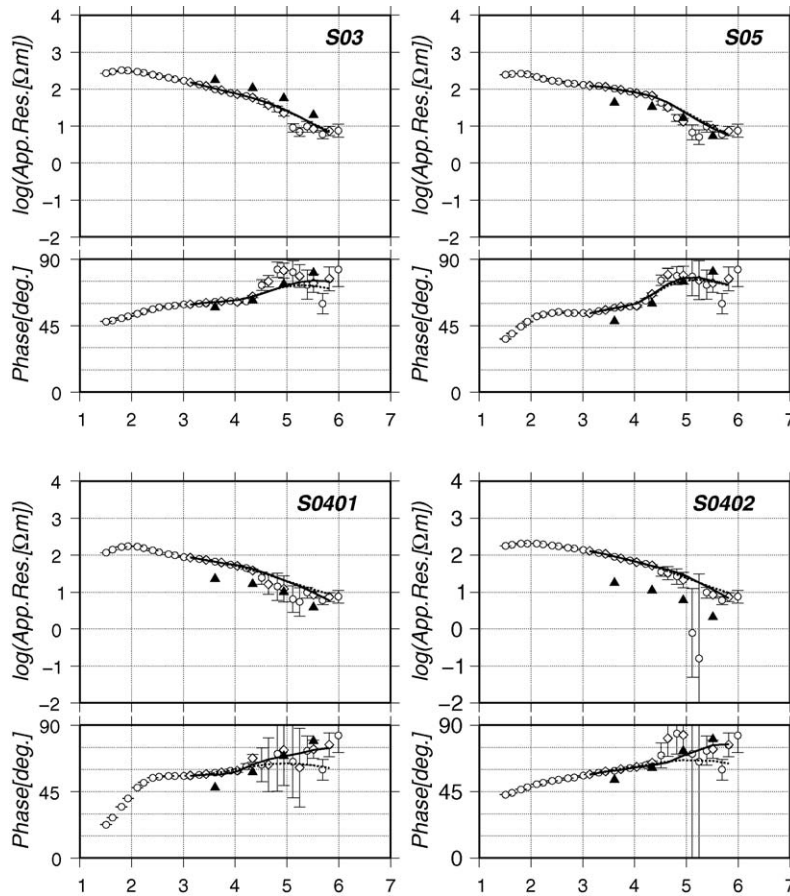


Fig. 5. Fitness between the EM responses observed and calculated from Fig. 4. Open circle and diamond symbols are observed EM data. Data shown by the diamond ones are used in the Occam inversion. The solid and dotted lines show the responses synthesized from the same lines in Fig. 4, respectively. Close triangle symbols represent the responses at 327,680, 87,380, 21,850 and 4096 s in period calculated from the model of Fig. 7. See text for details.

cates, we referred to the data of Xu et al. (2000). For the mixing law, we used Hashin–Shtrikman (H–S) bounds for conductivity (Park and Ducea, 2003):

$$\sigma_{\text{HS}} = \sigma_m + \frac{A_m}{1 - (A_m/3\sigma_m)} \quad (2)$$

$$A_m = \sum_i^{n-1} \frac{f_i}{(\sigma_i - \sigma_m)^{-1} + (3\sigma_m)^{-1}}, \quad (3)$$

where σ_{HS} means the H–S lower or upper bound. When $m = \text{minimum}$, σ_{HS} becomes H–S lower bound. When $m = \text{maximum}$, σ_{HS} becomes H–S upper bound. The bracket of the summation means excluding the index of the phase whose conductivity is maximum or minimum. f_i and σ_i represent volume fraction and conductivity of each silicate, respectively.

Fig. 10 shows a seismic P-wave velocity (V_p) perturbation structure beneath the Pacific back-arc, which is

updated by a newly developed parameterization method for whole mantle tomography (Obayashi and Fukao, 2001). The block size is determined depending on the resolution expected from the density of ray paths and the associated Fresnel zone size. The block size around NEC is laterally about 1.4° and radially 50–60 km at between 200 and 400 km in depth. About five million ray paths from 54,000 earthquakes occurring between 1964 and 1997 were used in the calculation. Note that the V_p perturbation is mostly negative down to 300 km in depth, and turns positive below 300 km beneath NEC.

In the following section, we attempt to quantify geotherm and water content profiles by using both conductivity and velocity structures based on the state-of-the-art laboratory experiments for silicates focusing on the upper mantle in the depth range between 200 and 400 km.

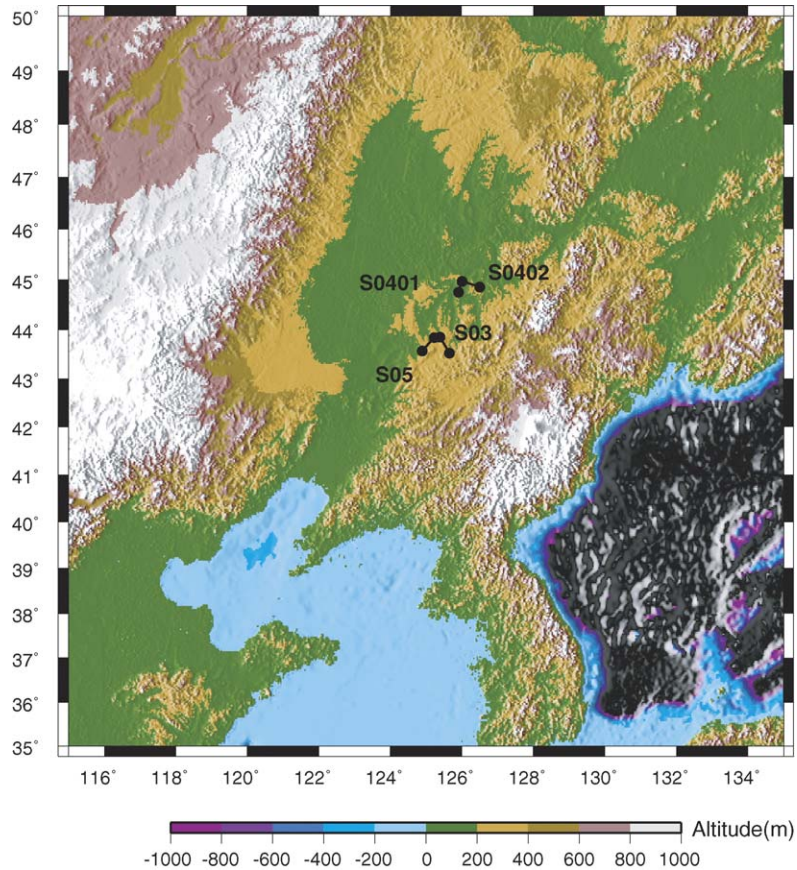


Fig. 6. Topographic map around the observation sites by the ETOPO2 data.

3. Quantitative interpretation of the electrical conductivity and seismic P-wave velocity structures

3.1. Electrical and seismic geotherms compared with petrological data

We first examined whether we were able to consistently interpret the conductivity and V_p structure assuming the dry condition. Namely, the mantle geotherm was estimated from the conductivity or V_p structures at 200–400 km in depth under the dry-condition (hereafter referred to as electrical and seismic geotherms). Pyrolite or harzburgite composition was allowed for in petrological composition, because we can interpret the upper mantle composition beneath NEC as a standard mantle or a harzburgite composition.

In estimating electrical and seismic geotherms, the Verhoogen effect (e.g., Schubert et al., 2001) and the volumetric change of composition generated by garnet-pyroxene transformation were neglected in this depth

range (e.g., Ito and Katsura, 1989). Electrical geotherm can be estimated straightforwardly:

- (1) The bulk conductivity of pyrolite or harzburgite is estimated at a given temperature by using Arrhenius law and H–S bounds described in the previous section.
- (2) Changing temperature in (1) by 10°C, electrical geotherm is estimated so as to coincide with the observed conductivity structures.

Seismic geotherm is calculated according to Vacher et al. (1996, 1998):

- (a) Density, ρ and elastic moduli, M (bulk modulus, K or shear modulus, G) of each silicate are calculated at a given temperature, T of the earth's surface.

$$\rho(T) = \rho(T_0) \exp \left[- \int_{T_0}^T \alpha(T') dT' \right] \quad (4)$$

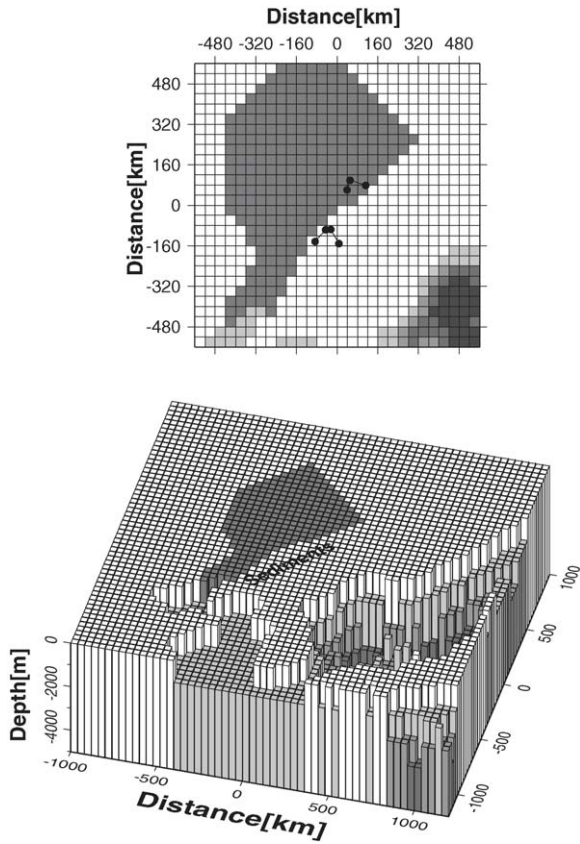


Fig. 7. Superficial conductive sediments distribution, discretized ocean bathymetry and gridding (bottom figure) used in the three dimensional modeling for testing the dimensionality. Conductivity of sea water was fixed at 3 S/m. Top is an enlarged figure around the observation sites. The shaded region represents the conductive sediments, the conductivity and the thickness of which were fixed at 1 S/m and 1 km, respectively.

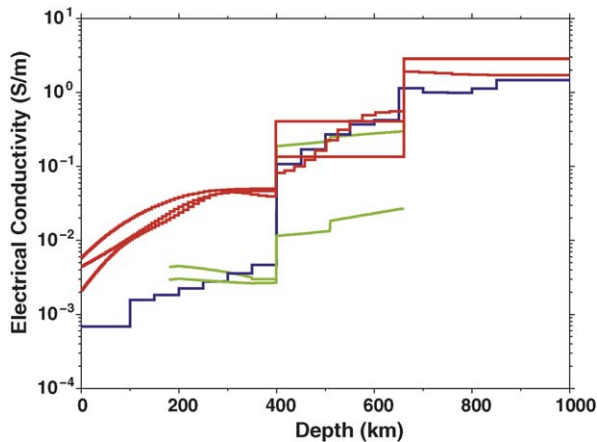


Fig. 8. Comparison among PBAs (red), FLDs (blue) and LABs (light green) models. Two lines of LABs are deduced from H–S lower and upper bounds, respectively.

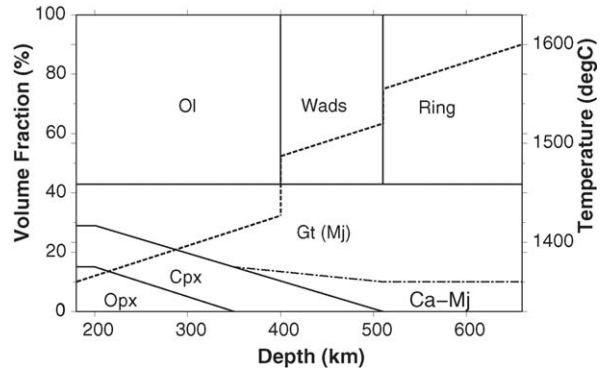


Fig. 9. Volumetric petrological composition of pyrolite. The broken line is a standard mantle geotherm used in the calculation of the conductivity profile (Xu et al., 2000; Turcotte and Schubert, 2002; Ito and Katsura, 1989). The temperature offsets at the boundaries of transformations represent the Verhoogen effect (e.g., Schubert et al., 2001). Abbreviations mean as follows; Ol: olivine, Wads: wadsleyite, Ring: ringwoodite, Gt (Mj): garnet (majorite), Ca-Mj: calcium majorite, Opx: orthopyroxene, Cpx: clinopyroxene.

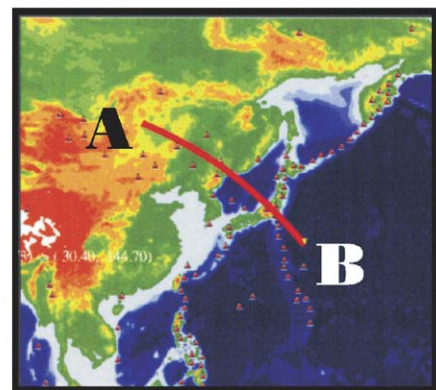
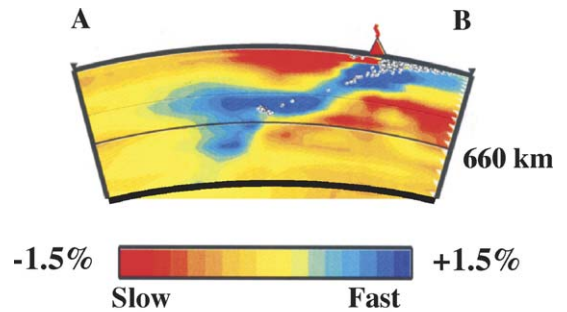


Fig. 10. Seismic P-wave velocity perturbation profile beneath the Pacific back-arc proposed by Obayashi and Fukao (2001). The reference model is regarded as ak135 (Kennet et al., 1995).

$$M(T) = M(T_0) \left[\frac{\rho(T)}{\rho(T_0)} \right]^{\{M\}_p} \quad (5)$$

$$M'(T) = M'(T_0) \exp \left[\int_{T_0}^T \alpha(T') dT' \right] \quad (6)$$

where α , M and M' represent thermal expansion coefficient, elastic moduli and pressure derivative of M , respectively. $\{M\}_p$ is dimensionless logarithmic anharmonic parameters (Anderson, 1988), which is assumed to be independent of temperature. The data set compiled in Vacher et al. (1998) was used for α and $\{M\}_p$.

- (b) Elastic moduli and their pressure derivatives for pyrolite or harzburgite composition are calculated using H–S bounds for elastic moduli (Vacher et al., 1996), which is defined as

$$M_{HS} = M_m + \frac{A_m}{1 - (A_m/3\beta_m)} \quad (7)$$

$$A_m = \sum_i^{n-1} \frac{f_i}{(M_i - M_m)^{-1} + (3\beta_m)^{-1}} \quad (8)$$

$$\beta_m = \frac{3K_m + 4G_m}{9} \quad (9)$$

M_{HS} means the H–S lower or upper bound. K_m is a minimum or a maximum bulk modulus and G_m is a minimum or a maximum shear modulus. Other notations are same as those in the case of conductivity.

- (c) Pyrolite or harzburgite V_p value under a pressure condition at a target depth is obtained by a finite strain provided by the second-ordered Birch–Murnagan's EOS (equation of state).

$$P = -3K\epsilon(1 - 2\epsilon)^{5/2} \left[1 + \frac{3}{2}(4 - K'\epsilon) \right] \quad (10)$$

$$\epsilon = \frac{1}{2} \left[1 - \left(\frac{\rho}{\rho_0} \right)^{2/3} \right] \quad (11)$$

$$\rho V_p^2 = (1 - 2\epsilon)^{5/2} (A + B\epsilon) \quad (12)$$

$$A = K + \frac{4}{3}G \quad (13)$$

$$B = 5A - 3KA' \quad (14)$$

where ϵ is a finite strain. Elastic moduli and their pressure derivatives are substituted into those obtained in (b). We applied PREM (Dziewonski and Anderson, 1981) to the pressure gage.

- (d) Simultaneously, the surface temperature given in (a) is also converted into temperature at the target

depth, T_{new} . We used a simplified adiabatic gradient (Turcotte and Schubert, 2002) described as

$$\left(\frac{\partial T}{\partial P} \right)_s = \frac{\gamma T}{K}, \quad (15)$$

where γ is the Grüneisen parameter. We can obtain the following equation by integrating the above equation with P :

$$T_{\text{new}} = T \exp \left(\gamma \int_0^P \frac{dP}{K} \right) \quad (16)$$

Sato (1995) revealed that dependency of the Grüneisen parameter on pressure is negligible in estimating the mantle geotherm. We applied 1.1 to the bulk Grüneisen parameter in both pyrolite and harzburgite compositions (e.g., Ita and Stixrude, 1993).

- (e) Changing temperature, T in (a) by 10 °C, the seismic geotherm via the procedure (d) is assessed so as to coincide with the observed V_p structures.

Fig. 11 shows an example of how to calculate the seismic geotherm. The solid line in the top of figure 11 is one profile of V_p structure beneath NEC. The dotted lines are velocity structures calculated along the adiabats, the surface temperature of which are 1450, 1550 and 1650 K, respectively, by the pyrolite composition in Fig. 9. Cpx and Ca-majorite are regarded as $(\text{Ca}_{0.5}\text{Mg}_{0.46}\text{Fe}_{0.04})\text{SiO}_3$ and grossular, since the effect of calcium in pyroxene and garnet on elastic moduli is crucial (e.g., Angel and Hugh-Jones, 1994; Hugh-Jones and Angel, 1997). Estimating from the top figure, the seismic geotherm is inferred as shown at the bottom of Fig. 11. The dotted lines are adiabats, the surface temperatures of which are 1450, 1550 and 1650 K, respectively. The two solid lines in the bottom of Fig. 11 are provided by H–S upper and lower bounds, respectively.

Note that the procedures to estimate electric and seismic geotherms are self-consistent. In order to verify the self-consistency, it is necessary to show that the seismic geotherm of the standard V_p structure under the pyrolite composition in Fig. 9 coincides with the standard geotherm, which is used in calculating electrical geotherm. Fig. 12 shows the velocity structure obtained by the pyrolite composition in Fig. 9. The calculated velocity structure along the 1550 K adiabat is consistent with ak135 (Kennet et al., 1995), which is applied to the standard V_p structure in estimating Fig. 10. Fig. 13 shows that the 1550 K adiabat is consistent with the standard geotherm adopted in the calculation of standard conductivity structure.

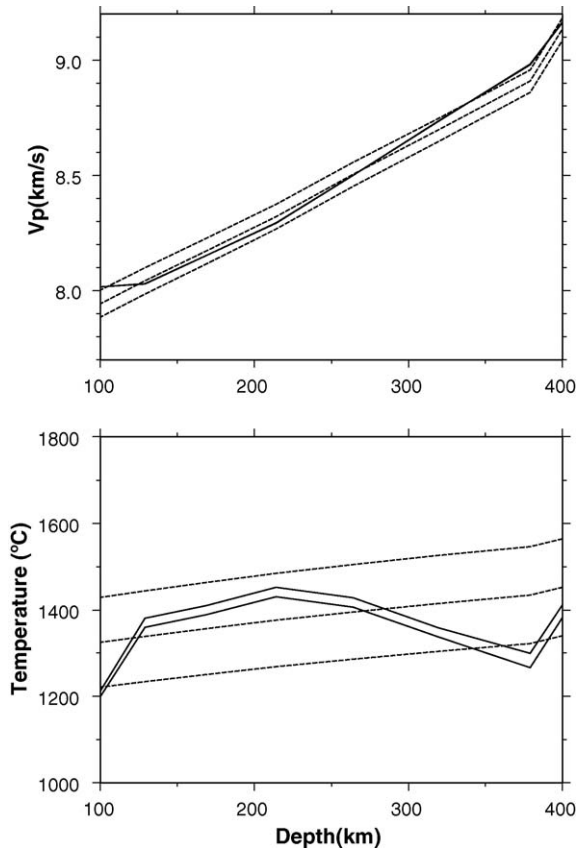


Fig. 11. Example to calculate seismic geotherm. Top: one of 16 V_p profiles is represented by the solid line. Dotted lines show the synthetic V_p profiles along adiabats that are 1450, 1550 and 1650 K at the earth's surface under the pyrolite composition of Fig. 9. Bottom: solid lines represent the seismic geotherm inferred from the top figure. Two solid lines mean the geotherms deduced from H–S lower and upper bounds. Dotted lines are adiabats, the surface temperatures of which are 1450, 1550 and 1650 K, respectively.

Fig. 14 represents the electrical (solid line) and seismic (broken lines) geotherms beneath NEC. The seismic geotherms are inferred from 16 vertical velocity structures in the region between $125 \pm 2.5^\circ$ in longitude and between $43.5 \pm 2.5^\circ$ in latitude, where the stagnant slab is embedded. Fig. 14 reveals that a significant discrepancy is found between the electrical and seismic geotherms in a deeper part of the upper mantle (below 300 km in depth). On the other hand, the discrepancy is smaller but still as large as over 100°C down to 250 km in depth.

Next, we calculated electrical and seismic geotherms with constraining petrological composition to a harzburgite (e.g., Irifune and Ringwood, 1987). We defined 20 vol% pyroxene (Opx above 300 km and Cpx below 300 km) and 80 vol% olivine as harzburgite composition. Fig. 15 shows the electrical and seismic geotherms under

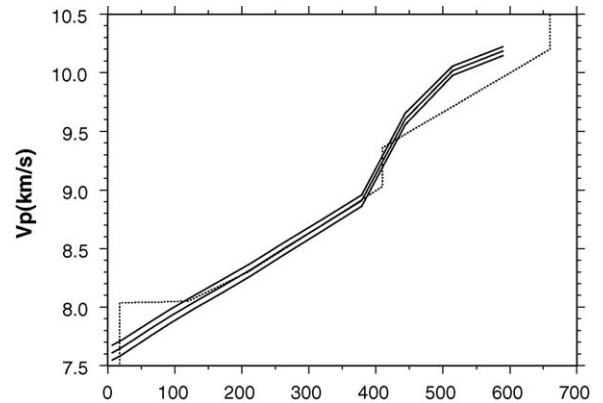


Fig. 12. Comparison between ak135 (Kennet et al., 1995) and synthetic V_p structures calculated from the pyrolite composition shown in Fig. 9. The dotted line indicate ak135 and the solid lines indicate synthetic V_p structures along the adiabats, the surface temperature of which are 1450, 1550 and 1650 K. The synthetic V_p structure along the 1550 K's adiabat is consistent with ak135.

the dry harzburgite composition. Good agreement was obtained between the seismic and electrical geotherms in a shallower part of the upper mantle down to 250 km in depth, although the dry harzburgite composition enlarged the discrepancy between electrical and seismic geotherms in a deeper part.

3.2. Water content

We attempted to account for the discrepancy between electrical and seismic geotherms by water or hydrogen dissolution in the mantle silicates, considering from the wet region hypothesis. Since V_p is little affected by small amount of water content in the mantle silicates (Karato, 1995, 1993), we regarded the seismic geotherm obtained

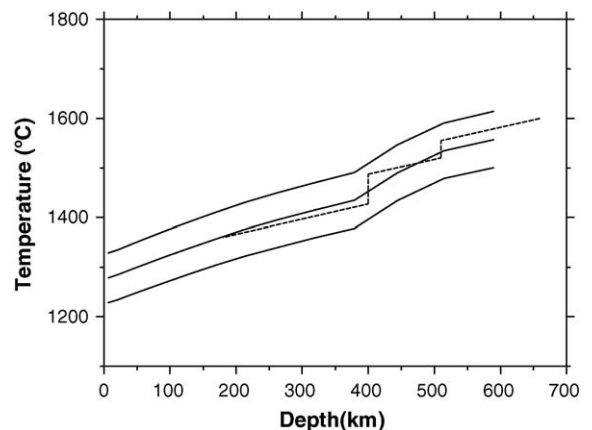


Fig. 13. Three adiabats whose surface temperatures are 1450, 1550 and 1650 K, respectively. The 1550 K's adiabat coincides with the standard mantle geotherm (broken line) shown in Fig. 9.

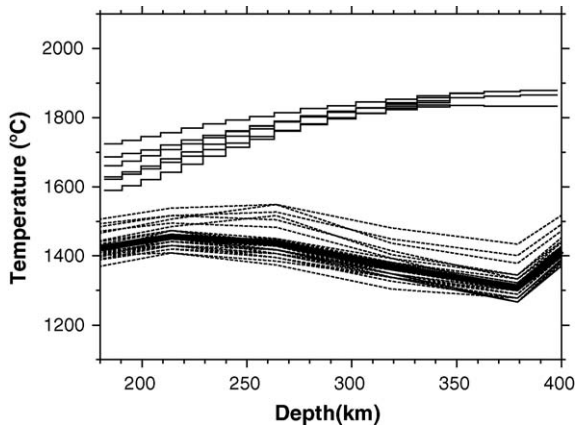


Fig. 14. Electrical (solid lines) and seismic geotherms (broken lines) beneath NEC under the pyrolite composition shown in Fig. 9. The thick broken line represents the average of 32 seismic geotherms (16 H–S lower and upper bounds).

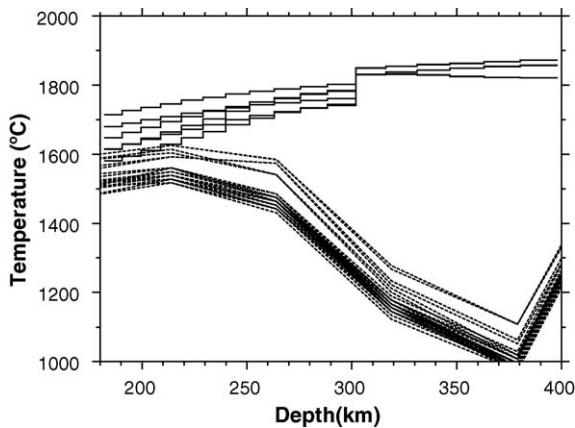


Fig. 15. Electrical (solid line) and seismic geotherms (broken lines) calculated from the harzburgite composition (20 vol% pyroxene and 80 vol% olivine).

by V_p structures as an appropriate mantle geotherm. The hydrogen content in silicates was estimated by electrical conductivity according to the hypothesis proposed by Karato (1990), in which dissolved hydrogen enhances electrical conductivity in the form of Nernst–Einstein relation. Table 1 gives experimental data on the hydrogen diffusion coefficients and the solubility for each silicate used in the estimation of water content. The moderate diffusion coefficients (asterisks in Table 1) for each silicate were used for calculation of water content, and anisotropy was not taken into account, because the EM data acquired in this region indicate one-dimensionality and no/weak intrinsic anisotropy. The partition coefficient of hydrogen dissolution in mantle silicates were taken into account. The concentration of hydrogen in cpx and opx were 10 and 5 times greater than that in olivine, respectively, and the concentration in garnet is as same as that in olivine (Hirth and Kohlstedt, 1996).

Fig. 16 represents the water content calculated from the conductivity structure of S03 using the averaged seismic geotherm. The water content is represented by the olivine-based value. The lower limit reveals that it is possible for water content of 70–700 ppm H/Si to realize the conductivity structure. For comparison, Fig. 16 also shows the water content calculated under a standard geothermal condition. If the standard geothermal profile is used, hydrogen dissolution in the deeper part of the upper mantle is estimated to be lower. Fig. 17 represents the calculated conductivity ranges with 500 and 1000 ppm H/Si water contents, respectively. The content of 500–1000 ppm H/Si is adequate to explain the conductivity structures. Since the effect of a small amount of water (~10,000 ppm H/Si) on seismic P-wave velocity in the upper mantle is negligibly small (Karato, 1995, 1993), the seismic geotherm and about 500–1000 ppm H/Si of water content adequately explain both the conductivity and V_p structures in the deeper part of the upper mantle.

Table 1
Hydrogen diffusion and solubility data

Silicates	Solubility (in ppm wt%)	Diffusion (in m^2/s)
Olivine	~ 1200 (~ 13 GPa, $1100^\circ C$) ^a	$D_a = (6 \pm 3) \times 10^{-5} \exp[-(130 \pm 30)/RT]^b$; $D_b \approx 10^{-2} D_a \approx 10^{-1} D_c^b$; * $D_c = (5 \pm 4) \times 10^{-6} \exp[-(130 \pm 30)/RT]^b$
Opx	867 ± 35 (7.5 GPa, $1100^\circ C$) ^c	* $D_c = 1.63 \times 10^{-5} \exp[-(161 \pm 17)/RT]^d$
Cpx	714 ± 35 (10 GPa, $1100^\circ C$) ^c	$D_a = 10^{-2.1 \pm 1.9} \exp[-(181 \pm 38)/RT]^e$; * $D_c = 10^{-3.4 \pm 1.6} \exp[-(153 \pm 32)/RT]^e$
Garnet	~ 200 (~ 10 GPa, $1000^\circ C$) ^f	* $D_{bulk} = 10^{0.282 \pm 0.567} \exp[-(253 \pm 13)/RT]^g$

^a Kohlstedt et al. (1996).

^b Mackwell and Kohlstedt (1990).

^c Rauch and Keppler (2002).

^d Woods and Mackwell (1999).

^e Woods et al. (2000).

^f Lu and Keppler (1997).

^g Wang et al. (1996).

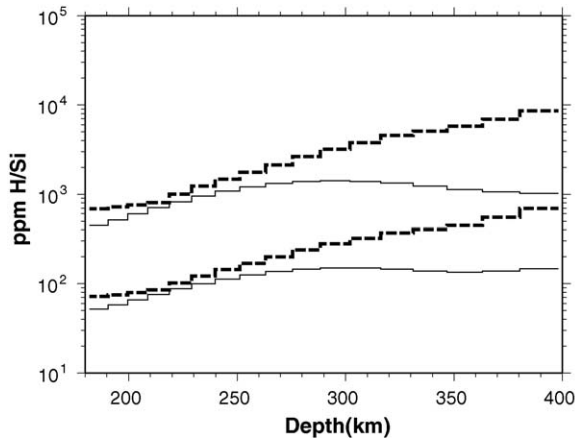


Fig. 16. Water content profiles estimated from the conductivity profile, S03 under the pyrolite composition. The solid line shows the data obtained under the standard temperature geotherm in Fig. 9. The thick broken line is obtained under the averaged seismic geotherm (the thick solid line in Fig. 14).

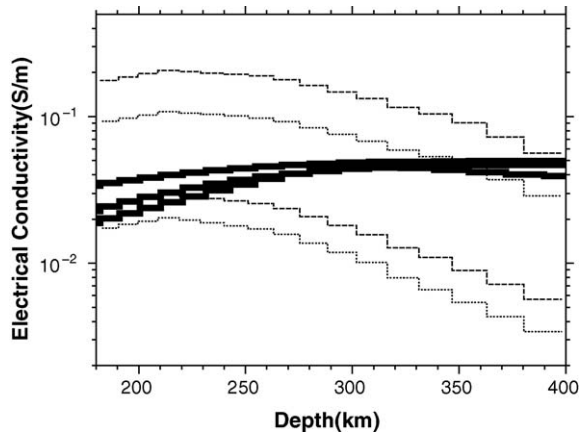


Fig. 17. Observed conductivity structure and synthetic conductivity profiles under the pyrolite composition and various water contents. Solid lines: observed conductivity profiles. Dotted lines: the conductivity of H–S upper and lower bounds under the water content of 500 ppm H/Si. Broken lines: the bounds under the water content of 1000 ppm H/Si.

4. Discussion

It is well known that the continental lithospheric mantle (CLM) beneath NEC is as thin as 70–150 km (Nohda et al., 1991; Xu, 2001; Yang et al., 2003). The conductivity and V_p structures used in this study have reliable resolution for the upper mantle beneath CLM, and revealed that the shallower part (200–250 km) of the upper mantle is different from the deeper part (\sim 250 km).

We can interpret the shallower part of the upper mantle as having a dry harzburgite composition or a wet pyrolite composition, alternatively, as described in the

previous section. Both EM and seismic data would show intrinsic anisotropy, when water exists in a region where olivine is arranged along a lattice preferred orientation. Oppositely, if water does not exist in such a region, seismic data would show intrinsic anisotropy, but EM data would show isotropy (Hirth et al., 2000). The upper mantle beneath NEC has shown clear seismic anisotropy (Iidaka and Niu, 2001) but no/weak electrical intrinsic anisotropy. However, since the depth range where the seismic anisotropy distributes is not well constrained, this result allows the alternative models for the shallower part depending on the depth range of the seismic anisotropy present. If most of the seismic anisotropy distributes in the CLM, we can interpret the shallower part as having a wet pyrolite composition. Otherwise, if the seismic anisotropy mostly exists beneath the CLM, the shallower part should be of dry harzburgite composition. The interpretation by dry harzburgite suggests that harzburgite exists in the uppermost asthenosphere, and the harzburgite plume hypothesis is supported as a result. However, such a lateral scale of the heterogeneity in the uppermost asthenosphere has not yet been imaged by seismic velocity and electrical conductivity structures.

The comparison described in the previous section shows that the electrical and seismic geotherms are significantly different from each other in the deeper part of the upper mantle under the dry pyrolite or the dry harzburgite composition. However, this discrepancy can be overcome by allowing for a amount of water over 500–1000 ppm H/Si. The effect of a small amount of water (\sim 10,000 ppm H/Si) on seismic P-wave velocity in the upper mantle is considered to be negligibly small (Karato, 1995, 1993) in contrast to that of electrical conductivity (Karato, 1990). Hence, we can interpret that the seismic geotherm reflects an adequate mantle geotherm as long as the water content in the upper mantle is small. On the other hand, the electrical conductivity structure can be explained by a small amount of water and the seismic geotherm. Therefore, we can conclude that the seismic geotherm and about 500–1000 ppm H/Si of water content adequately explain both the conductivity and V_p structures in the deeper part of the upper mantle. This result suggests that the wet region hypothesis is appropriate for the deeper part of the upper mantle. However, the confidence width of amount of water in the deeper part is constrained in this study.

Consequently, our alternative models for the upper mantle beneath NEC can be illustrated as shown in Fig. 18. The first model extensively explains the upper mantle by the wet region hypothesis (top of Fig. 18). Following this model, it is necessary that the origin of the observed seismic anisotropy exist in the CLM. The second model

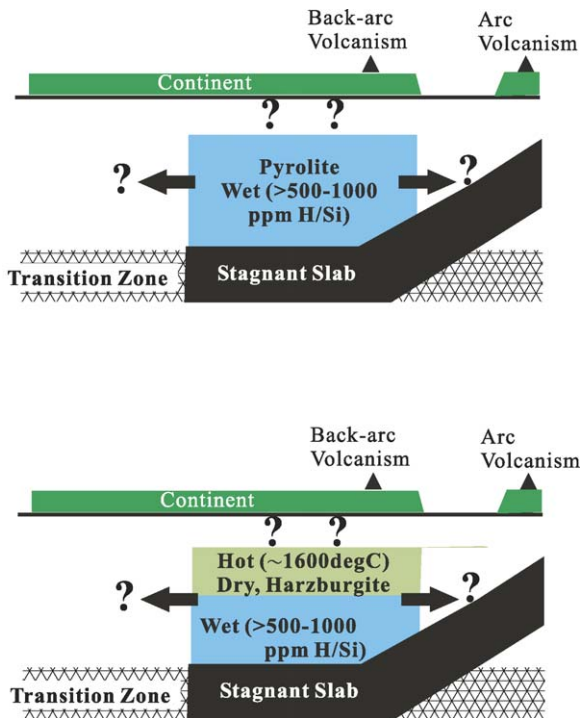


Fig. 18. Alternative models proposed to the upper mantle beneath the Pacific back-arc. See text for details.

explains the deeper part of the upper mantle by the wet region hypothesis, and the shallower part by the hot and harzburgite plume hypotheses, respectively (bottom of Fig. 18). Detection of the depth range, where the origin of the seismic anisotropy is embedded, is required to determine the appropriate model from the alternative.

We did not estimate seismic geotherm by using V_s . Because the resolution of the V_p structure is inferior to that of V_s and the V_s is supposed not to be estimated accurately by the procedure of Vacher et al. (1996, 1998), which mainly estimates the anharmonic effect of the elastic wave velocity of the silicates. V_s are equally controlled by anharmonic and anelastic effects and the laboratory experiments used in the procedure of Vacher et al. (1996, 1998) was mainly carried out in the high frequencies, where anharmonic effect is dominant (Karato, 1993). Actually, Vacher et al. (1996) reported that the correlation between synthetic and observed V_s structures was worse than that between synthetic and observed V_p structure. This is because the procedure of Vacher et al. (1996, 1998) estimates only the anharmonic effect of V_s . V_p is mainly controlled by the anharmonic effect and the V_p values calculated by using laboratory data collected in the high frequencies are expected to be appropriate.

In this paper, the $Mg/(Mg + Fe)$ ratio was assumed to be 0.9 in olivine and garnet and 0.92 in pyroxene.

The chemical composition (e.g., $Mg/(Mg + Fe)$ ratio) of each silicate is essentially controlled by oxidation state or oxygen fugacity and is expected to affect conductivity by generating polaron. The subduction zone is expected to be a relatively oxidized region (e.g., Wood et al., 1990). Recent studies of xenoliths have begun to elucidate the quantitative oxidation states in the upper mantle of various tectonic settings (Johnson et al., 1996). However, the influence of the chemical composition of each silicate on conductivity has not yet been sufficiently investigated. Even the influence of the $Mg/(Mg + Fe)$ ratio on conductivity of pyroxenes is not well understood (Xu and Shankland, 1999). Consequently, investigative methods are as yet not able to estimate quantitative anomaly of chemical composition from conductivity structure.

5. Conclusion

We investigated temperature and water content in the upper mantle beneath the northeastern part of China in the Pacific back-arc by comparing electrical conductivity and seismic P-wave velocity structure. Our conclusions were as follows:

- (1) In the deeper part of the upper mantle, the electrical and seismic geotherms are significantly different from each other under a dry pyrolite or a dry harzburgite composition. However, even a small amount of water over 500 ppm H/Si could account for the electrical conductivity structure when using the seismic geotherm and the pyrolite composition, although water content is not well constrained. This result implies that the deeper part of the upper mantle beneath the Pacific back-arc is naturally under the wet condition.
- (2) We can interpret the shallower part of the upper mantle alternatively as a dry harzburgite composition or a wet pyrolite composition. The electrical and seismic geotherms are consistent with each other under a dry harzburgite composition, whereas a dry pyrolite composition cannot consistently explain the electrical conductivity and seismic velocity structures in the shallower part of the upper mantle. However, a wet pyrolite condition can be applied to the shallower part of the upper mantle beneath the northeastern part of China. The more appropriate of the two models can be determined by investigating the depth range where the origin of the seismic anisotropy is embedded. More quantitative analysis of electrical intrinsic anisotropy will be useful for solving this problem, which requires EM data of much higher quality.

Acknowledgements

Drs. Tomoo Katsura Kiyoshi Fuji-ta and Hisayoshi Shimizu gave insightful discussions and critical reading of manuscript. Drs. Shigeaki Ono, Daisuke Suetsugu, Takao Koyama, Yoshio Nishio, Natsue Abe, Tetsu Kogiso, Yoshiyuki Tatsumi, Alessandro Forte and Takeshi Hanyu gave useful comments. The authors also thank Dr. J. Tyburczy and an anonymous referee for their constructive comments that greatly improved the paper. Several figures were created using the free software GMT (Wessel and Smith, 2003). Drs. Makoto Uyeshima and Alan Chave allowed us to use their modeling and analysing programs.

References

- Akaogi, M., Navrotsky, A., Yagi, T., Akimoto, S., 1987. Pyroxene-garnet transformation: thermochemistry and elasticity of garnet solid solutions, and application to a pyrolyte mantle. In: Mangh-nani, M.H., Syono, Y. (Eds.), *High-pressure Research in Mineral Physics*. Terra Scientific Publishing Co. Ltd., Tokyo 251–260.
- Anderson, D.L., 1988. Temperature and pressure derivatives of elastic constants with application to the mantle. *J. Geophys. Res.* 93, 4688–4700.
- Angel, R.J., Hugh-Jones, D.A., 1994. Equations of state and thermodynamic properties of enstatite pyroxenes. *J. Geophys. Res.* 99, 19777–19783.
- Bijwaard, H., Spakman, W., Engdahl, E.R., 1998. Closing the gap between regional and global travel time tomography. *J. Geophys. Res.* 103, 30055–30078.
- Chave, A.D., Thomson, D.J., Ander, M.E., 1987. On the robust estimation of power spectra, coherences and transfer functions. *J. Geophys. Res.* 92, 633–648.
- Constable, S.C., Parker, R.L., Constable, C.G., 1987. Occam's inversion: A practical algorithm for generating smooth models from electromagnetic sounding data. *Geophysics* 52, 289–300.
- Duffy, T.S., Anderson, D.L., 1989. Seismic velocities in mantle minerals and the mineralogy of the upper mantle. *J. Geophys. Res.* 94, 1895–1912.
- Dziewonski, A.M., Anderson, D.L., 1981. Preliminary reference Earth model. *Phys. Earth Planet. Int.* 25, 297–356.
- Fukao, Y., Koyama, T., Obayashi, M., Utada, H., 2004. Trans-Pacific temperature field in the mantle transition region derived from seismic and electromagnetic tomography. *Earth Planet. Sci. Lett.* 217, 425–434.
- Fukao, Y., Widiyantoro, S., Obayashi, M., 2001. Stagnant slabs in the upper and lower mantle transition region. *Rev. Geophys.* 39, 291–323.
- Fukao, Y., Obayashi, M., Inoue, H., Nenbai, M., 1992. Subducting slabs stagnant in the mantle transition zone. *J. Geophys. Res.* 97, 4809–4822.
- Hirth, G., Evans, R.L., Chave, A.D., 2000. Comparison of continental and oceanic mantle electrical conductivity: Is the Archean lithosphere dry?. *Geochem. Geophys. Geosyst.* 1 2000GC000048.
- Hirth, G., Kohlstedt, D.L., 1996. Water in the oceanic upper mantle: implications for rheology, melt extraction and the evolution of the lithosphere. *Earth Planet. Sci. Lett.* 144, 93–108.
- Hugh-Jones, D.A., Angel, R.J., 1997. Effect of Ca^{2+} and Fe^{2+} on the equation of state of MgSiO_3 orthopyroxene. *J. Geophys. Res.* 102, 12333–12340.
- Ichiki, M., Uyeshima, M., Utada, H., Zhao, G., Tang, J., Ma, M., 2001. Upper mantle conductivity structure of the back-arc region beneath northeastern China. *Geophys. Res. Lett.* 28, 3773–3776.
- Iidaka, T., Niu, F., 2001. Mantle and crust anisotropy in the eastern China region inferred from waveform splitting of SKS and PpSms. *Earth Planets Space* 53 159–168.
- Irifune, T., Sekine, T., Ringwood, A.E., Hibberson, W.O., 1986. The eclogite-garnetite transformation at high pressure and some geophysical implications. *Earth Planet. Sci. Lett.* 77, 245–256.
- Irifune, T., Ringwood, A.E., 1987. Phase transformations in hartzburgite composition to 26 GPa: implications for dynamical behaviour of the subducting slab. *Earth Planet. Sci. Lett.* 86, 365–376.
- Ita, J., Stixrude, L., 1993. Density and elasticity of model upper mantle compositions and their implications for whole mantle structure. In: Takahashi, E., Jeanloz, R., Rubie, D. (Eds.), *Evolution of the Earth and Planets*. Am. Geophys. Union 111–130.
- Ito, E., Katsura, T., 1989. A temperature profile of the mantle transition zone. *Geophys. Res. Lett.* 16, 425–428.
- Iwamori, H., 1992. Degree of melting and source composition of Cenozoic basalts in southwestern Japan: evidence for mantle upwelling by flux melting. *J. Geophys. Res.* 97, 10983–10995.
- Johnson, K.E., Davis, A.M., Bryndzia, L.T., 1996. Contrasting styles of hydrous metasomatism in the upper mantle: An ion microprobe investigation. *Geochim. Cosmochim. Acta* 60, 1367–1385.
- Karato, S.-I., 1995. Effects of water on seismic wave velocities in the upper mantle. *Proc. Jpn. Acad.* 71 (B), 61–66.
- Karato, S.-I., 1993. Importance of anelasticity in the interpretation of seismic tomography. *Geophys. Res. Lett.* 20, 1623–1626.
- Karato, S.-I., 1990. The role of hydrogen in the electrical conductivity of the upper mantle. *Nature* 347, 272–273.
- Kennet, B.L.N., Engdahl, E.R., Buland, R., 1995. Constraints on seismic velocities in the Earth from traveltimes. *Geophys. J. Int.* 122, 108–124.
- Kohlstedt, D.L., Keppler, H., Rubie, D.C., 1996. Solubility of water in the α , β , γ phases of $(\text{Mg,Fe})_2\text{SiO}_4$. *Contrib. Mineral. Petrol.* 123, 345–357.
- Kuvshinov, A., Utada, H., Avdeev, D., Koyama, T., 2005. 3-D modeling and analysis of the Dst C-responses in the North Pacific Ocean region revisited. *Geophys. J. Int.* 160, 505–526.
- Lu, R., Keppler, H., 1997. Water solubility in pyrope to 100 kbar. *Contrib. Mineral. Petrol.* 129, 35–42.
- Mackie, R.L., Smith, J.T., Madden, T.R., 1994. Three-dimensional electromagnetic modeling using finite difference equations: the magnetotelluric example. *Radio Sci.* 29, 923–935.
- Mackwell, S.J., Kohlstedt, D.L., 1990. Diffusion of hydrogen in olivine: implications for water in the mantle. *J. Geophys. Res.* 95, 5079–5088.
- Miyashiro, A., 1986. Hot regions and the origin of marginal basins in the western pacific. *Tectonophysics* 122, 195–216.
- Nohda, S., Chen, H., Tatsumi, Y., 1991. Geochemical stratification in the upper mantle beneath NE China. *Geophys. Res. Lett.* 18, 97–100.
- Obayashi, M. and Fukao, Y., 2001. Whole mantle tomography with an automatic block parameterization. *Proceedings of Seis Soc. Japan fall meeting* (in Japanese).
- Poe, B.T., Romano, C., Kreidie, N., McCammon, C.A., 2002. Electrical conductivity of garnets: the effect of Fe–Mg substitution in the system pyrope ($\text{Mg}_3\text{Al}_2\text{Si}_3\text{O}_8$)–almandine ($\text{Fe}_3\text{Al}_2\text{Si}_3\text{O}_8$).

- Bayrisches Forschungsinstitut für Experimentelle Geochemie und Geophysik, Annual report. <http://www.bgi.uni-bayreuth.de>.
- Park, S.K., Ducea, M.N., 2003. Can in situ measurements of mantle electrical conductivity be used to infer properties of partial melts? *J. Geophys. Res.* 108, 2270. doi:10.1029/2002JB001899.
- Rauch, M., Keppler, H., 2002. Water solubility in orthopyroxene. *Contrib. Mineral. Petrol.* 143, 525–536.
- Ringwood, A.E., 1975. *Composition and Petrology of the Earth's Mantle*. McGraw-Hill, New York, 618 pp.
- Sato, H., 1995. Seismic velocity at mantle solidus temperature: implications for the thermal structure of the low velocity zone. *Zisin* 48, 131–137 (in Japanese with English abstract).
- Schubert, G., Turcotte, D.L., Olson, P., 2001. *Mantle Convection in the Earth and Planets*. Cambridge Univ. Press, London 940 pp.
- Schultz, A., Larsen, J.C., 1987. On the electrical conductivity of the mid-mantle: I. Calculation of equivalent scalar magnetotelluric response functions. *Geophys. J. Roy. Astr. Soc.* 88, 733–761.
- Tatsumi, Y., Eggins, S., 1995. *Subduction Zone Magmatism*. Blackwell Science, London 211 pp.
- Turcotte, D.L., Schubert, G., 2002. *Geodynamics*. Cambridge Univ. Press, London 456 pp.
- Utada, H., Koyama, T., Shimizu, H., Chave, A.D., 2003. A semi-global reference model for electrical conductivity in the mid-mantle beneath the north Pacific region. *Geophys. Res. Lett.* 30, 1194. doi:10.1029/2002GL016092.
- Uyeshima, M., Utada, H., Nishida, Y., 2001. Network-MT method and its first results in Central and Eastern Hokkaido. *Geophys. J. Int.* 146, 1–19.
- Vacher, P., Mocquet, A., Sotin, C., 1998. Computation of seismic profiles from mineral physics: the importance of the non-olivine components for explaining the 660 km depth discontinuity. *Phys. Earth Planet. Int.* 106, 275–298.
- Vacher, P., Mocquet, A., Sotin, C., 1996. Comparison between tomographic structures and models of convection in the upper mantle. *Geophys. J. Int.* 124, 45–56.
- van der Hilst, R.D., Engdahl, R., Spakman, W., Nolet, G., 1991. Tomographic imaging of subducted lithosphere below northwest Pacific island arcs. *Nature* 353, 37–43.
- Wang, L., Zhang, Y., Essene, E.J., 1996. Diffusion of the hydrous component in pyrope. *Am. Mineral.* 81, 706–718.
- Wessel, P., Smith, W.H.F., 2003. The generic mapping tools, GMT. <http://gmt.soest.hawaii.edu/>.
- Wood, B.J., Bryndzia, L.T., Johnson, K.E., 1990. Mantle oxidation state and its relationship to tectonic environment and fluid speciation. *Science* 248, 337–345.
- Woods, S.C., Mackwell, S., Dyar, D., 2000. Hydrogen in diopside: diffusion profiles. *Am. Mineral.* 85, 480–487.
- Woods, S.C., Mackwell, S., 1999. Hydrogen diffusion in enstatite. Bayrisches Forschungsinstitut für Experimentelle Geochemie und Geophysik, Annual report. <http://www.bgi.uni-bayreuth.de>.
- Xu, Y., Poe, B.T., Shankland, T.J., Rubie, D.C., 1998. Electrical conductivity olivine, wadsleyite, and ringwoodite under upper mantle condition. *Science* 280, 1415–1418.
- Xu, Y., Shankland, T.J., 1999. Electrical conductivity of orthopyroxene and its high pressure phases. *Geophys. Res. Lett.* 26, 2645–2648.
- Xu, Y., Shankland, T.J., Poe, B.T., 2000. Laboratory-based electrical conductivity in the Earth's mantle. *J. Geophys. Res.* 105, 27865–27875.
- Xu, Y.-G., 2001. Thermo-tectonic destruction of the archaean lithospheric keel beneath the Sino-Korean craton in China: Evidence, timing and mechanism. *Phys. Chem. Earth (A)* 26, 747–757.
- Yang, J.-H., Wu, F.-Y., Wilde, S.A., 2003. A review of the geodynamic setting of large-scale late Mesozoic gold mineralization in the north China craton: an association with lithospheric thinning. *Ore Geol. Rev.* 23, 125–152.